Masking effect of surface coatings in long pulsed thermography: A quantitative analysis of thickness discrimination

Optics and Lasers in Engineering 196 (2026) 109400

Contents lists available at ScienceDirect

Optics and Lasers in Engineering

journal homepage: www.elsevier.com/locate/optlaseng

Masking effect of surface coatings in long pulsed thermography: A quantitative analysis of thickness discrimination

Raffaella Sesana [1], Luca Santoro [1], Ludovica Tromba [*]

Department of Mechanical and Aerospace Engineering, Politecnico di Torino, Corso Duca degli Abruzzi 24, Torino, 10129, Italy

ARTICLE INFO

Keywords:
Active thermography
Laser-long pulse thermography
Emissivity
Thickness discrimination
Black paint

ABSTRACT

Active thermography is a powerful non-destructive evaluation (NDE) technique for characterizing materials and detecting defects. A common practice to enhance measurement reliability is the application of a high-emissivity paint coating. However, this coating can introduce a thermal barrier, potentially masking the intrinsic thermal response of the underlying substrate, which is critical for tasks such as thickness discrimination. This study provides a quantitative analysis of the masking effect induced by a black paint coating on the transient thermal response of steel samples of varying thicknesses, as measured by laser-long pulse active thermography. We employ a combined approach of analytical modeling, numerical simulation, and experimental validation. The analysis is grounded in the one-dimensional heat conduction equation, with a lumped-parameter model used to explore the system's primary dynamics. Experimental tests on a multi-thickness steel block provide validation data. Our findings reveal that the low thermal diffusivity of the paint layer creates a significant initial thermal transient that can obscure the thickness-dependent response of the substrate. This masking effect is particularly pronounced for thicker coatings and substrates. We demonstrate that spatial averaging of the thermal data can partially mitigate this effect, restoring thickness discrimination for substrates up to a certain thickness threshold. The study concludes that while emissivity-enhancing coatings are beneficial, their thermal properties must be carefully considered in the design and interpretation of long pulsed thermography experiments. We propose practical guidelines for optimizing coating selection and data analysis strategies to preserve the integrity of NDE measurements.

1. Introduction

Infrared (IR) thermography is a versatile and non-destructive evaluation (NDE) technique that enables full-field, contactless temperature measurement of component surfaces. By capturing the emitted thermal radiation, thermography can infer subsurface features, detect damage, and assess material properties such as thermal diffusivity, conductivity, and emissivity [1–13]. This capability has proven invaluable in industries as diverse as aerospace, automotive, and civil engineering, where ensuring structural integrity and reliability is paramount.

Active thermography, in which an external heat source (e.g., flash lamps, halogen lamps, laser beams) is used to stimulate the specimen, provides dynamic thermal responses which can be analyzed to detect subsurface defects or material inhomogeneities [8,14–16]. Among active thermographic techniques, laser-long pulse thermography—or laser spot thermography—offers the advantage of highly localized heating and potentially superior spatial resolution [17–25]. This is particularly useful for evaluating thin layers, complex geometries, and advanced materials, including fiber-reinforced polymers and metals produced via additive manufacturing [7,26–30].

A critical challenge in thermographic measurements is the variability of surface emissivity. Real surfaces rarely behave as ideal blackbodies. Instead, their emissivity depends on factors such as surface roughness, oxidation, coatings, or material composition [31–33]. To address this, a common practice is to apply a black paint coating to standardize and increase emissivity, thereby enhancing measurement accuracy and repeatability [10–12,26,34]. This practice is recommended in Standards as [35,36]. Similar practices in the literature use graphite sprays and surface roughening to reduce reflectance [37][38]. While beneficial in passive thermography and slower thermal phenomena evaluation [39], the presence of a paint coating in active thermography can introduce complexities. In particular, the paint layer acts as an intermediate ther-

* Corresponding author.
E-mail addresses: raffaella.sesana@polito.it (R. Sesana), luca.santoro@polito.it (L. Santoro), ludovica.tromba@polito.it (L. Tromba).
[1] Contributing authors.

https://doi.org/10.1016/j.optlaseng.2025.109400
Received 21 July 2025; Received in revised form 15 September 2025; Accepted 9 October 2025

Available online 14 October 2025

mal resistor and capacitor, altering the initial heating transient and potentially obscuring thickness-dependent thermal responses [22,40–43]. A correct analysis of material response is critical for material physical parameters as for example local sample diffusivity. This parameter allows the assessment of many critical information as for example microstructural conditions, local fatigue damage evaluation, defect detections both in metal and polymeric based materials. Thickness discrimination is central to several NDE tasks, such as evaluating weld nugget size in resistance spot welded (RSW) joints, detecting subsurface flaws in welded structures, or characterizing the thermal and mechanical properties of additively manufactured parts. Welded joints are crucial in automotive and aerospace sectors, and their integrity depends on accurate assessment of weld quality. Emerging research has focused on employing active thermography to evaluate weld quality, including RSW joints, correlating thermographic signatures with mechanical properties like maximum tensile resistance and nugget diameter [15,16,27,40].

For instance, thermographic approaches have been applied to resistance projection welded (RPW) joints, additive manufactured steels, and complex welding processes, showing that careful data processing and calibration can restore some thickness discrimination capability even when coatings are present [14,44–49]. These studies have shown that by integrating thermographic data with finite element simulations, inverse heat conduction methods, and advanced signal processing algorithms, such as least squares fitting, sparse principal components, and machine learning approaches, it is possible to partially overcome the distortions introduced by paint coatings [3,7,13,21,23,33,50–55].

Non-destructive testing (NDT) of welded joints, additive manufactured components, and composite materials can benefit from refined thermographic techniques. By understanding how paint coatings affect transient temperature fields and identifying strategies to mitigate these effects — such as spatial averaging, later-time data analysis, or model-based corrections — engineers can maintain or even improve thickness discrimination capability. In turn, this bolsters quality assurance processes, reduces inspection time and costs, and ensures safer, more reliable components in critical industries.

This study systematically investigates the influence of black paint coatings on the ability of laser-long pulse active thermography to discriminate substrate thickness. By combining analytical modeling, numerical simulations, and experimental tests on steel samples, we explore the complex interplay between paint thickness, substrate thickness, and the resulting thermal transient. We demonstrate that while spatial averaging and analysis of the cooling phase can partially recover thickness-dependent information, the masking effect of the coating imposes fundamental limits on the technique's sensitivity. The insights derived are critical not only for thickness gauging but also for broader NDE applications, including defect detection and material characterization, where coatings are prevalent [56–58].

The remainder of this paper is structured as follows. Section 2 details the theoretical framework, the numerical model, and the experimental setup. Section 3 presents and discusses the simulation and experimental results. Section 4 provides an extended discussion on the practical implications of our findings, and Section 5 concludes the paper with a summary of the key contributions and guidelines for practitioners.

2. Material and methods

The transient thermal behavior of a flat metal slab coated by a black paint, undergoing the energy input of a laser long pulse can be described by the one-dimensional heat conduction equation, which governs heat flow through the paint and steel layers:

$$\frac{\partial T(x,t)}{\partial t} = \alpha \frac{\partial^2 T(x,t)}{\partial x^2} \tag{1}$$

where $T(x,t)$ is the temperature at position x and time t, and $\alpha = k/(\rho c)$ is the thermal diffusivity, with k being the thermal conductivity, ρ the density, and c the specific heat capacity. The laser long pulse provides a heat flux q_0 at the surface ($x = 0$), while continuity of temperature and heat flux is maintained at the paint-steel interface.

Table 1
Properties and nominal specific heats for steel and paint.

Material	Density (kg/m^3)	Conductivity (W/m K)	Spec. Heat (J/kg K)	Thickness Range (m)
Steel	7850	60.5	490	0.0025–0.01
Paint	1200	0.25	1300	1e-5–0.01

For this analysis, a simplified analytical lumped-parameter model was developed. This approach is justified when the internal thermal resistance of a body is negligible compared to its external convective resistance, a condition quantified by the Biot number:

$$Bi = \frac{hL_c}{k} \tag{2}$$

where h is the convective heat transfer coefficient, L_c is the characteristic length, and k is the thermal conductivity. For thin layers and short transients, where $Bi \ll 1$, temperature gradients within each layer can be considered negligible, validating the use of a lumped model.

The model calibration was obtained by means of literature data (Table 1) and model validation was then conducted by experimental testing. To this aim, a series of active laser long pulse thermography tests were conducted on a steel calibration block with various thicknesses, on which a layer of black paint had been applied and distributed evenly.

2.1. Lumped-parameter model

To capture the primary dynamics of the system, a lumped-capacity model was implemented in MATLAB®/Simulink® (Fig. 1). This model simplifies the distributed thermal response described by Eq. (1) into a system of ordinary differential equations, which is computationally efficient for parametric studies. A constant heat flux, representing the laser power P over a time interval δt, is applied to the external surface of the paint layer, thus simulating a square wave energy input. Each layer (paint and steel) is treated as a distinct thermal mass arranged in series, characterized by its thermal resistance and capacitance. The paint layer absorbs the initial energy and subsequently acts as a thermal source for the underlying steel, thereby conditioning the substrate's thermal transient. The lumped parameter model considers an average energy in time and space while the experimental reality is Gaussian distribution in space and the presence of transients in time. The core assumption of this model is that the temperature within each lumped mass is spatially uniform at any given time, that is the model is 0D in space. The *thermal capacity* of each layer is defined in the Simulink model by its mass and specific heat, which together determine the total heat capacity of the thermal mass block.

The thermal input can be described in terms of incremental heat δq and incremental temperature δT, according to:

$$\delta q = C\,\delta T \tag{3}$$

where C is the heat capacity. By also noting that the incremental heat over a time interval δt can be expressed as

$$\delta q = P\,\delta t \tag{4}$$

with P representing the power of the energy input, the heat accumulation in the component can be approximated. Equating the two expressions (3) and (4) yields:

$$\frac{\delta q}{\delta t} = P = C\,\frac{\delta T}{\delta t} \tag{5}$$

since P is assumed constant during the laser long pulse, the heating process exhibits a linear behavior.

Heat capacity is an extensive property related to the specific heat capacity c and the mass of the material. We assume the specimen large

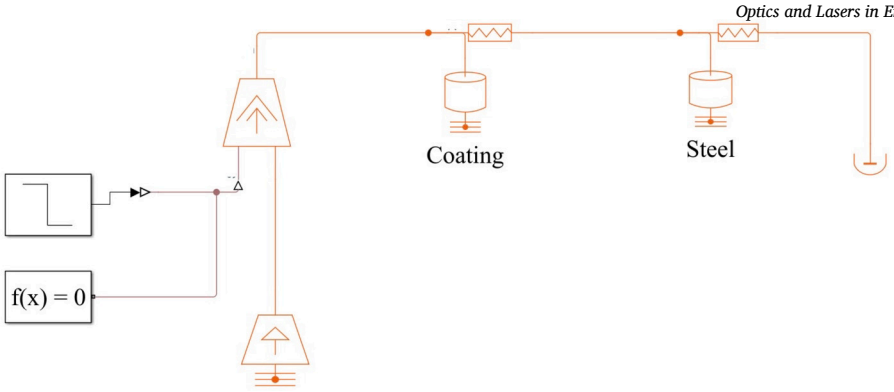

Fig. 1. Simplified lumped parameter model representing coating (paint) and steel layers.

as the region of interest from the thermal measurements. For a given cross-sectional area A and thickness s, the total heat capacity is

$$C = c\,A\,s \tag{6}$$

and for small paint layers with short transients, one can express the heating rate dependence on thickness as

$$\frac{\delta T}{\delta t} = \frac{P}{A\,c\,s} \tag{7}$$

The Simulink model therefore represents steel and paint as separate blocks. Each block has user-defined parameters for density, specific heat, and thickness, from which Simscape® computes the total thermal capacity. By systematically varying these thicknesses and properties, the model investigates how thermal energy propagates in the paint coating to reach the steel layer, and then how heat penetration is delayed and how the steel substrate thickness affects its own temperature evolution. The simulation outputs provide temperature-rise curves for both layers, allowing comparisons across different thickness configurations. In Table 1 the calibration values of the model parameters are reported. These calibration values are obtained from literature [59,60].

Environment conditions in the model fix the temperature at 293.15 K, and a constant heat flux is imposed over a selected duration. Convective heat flow is negligible according to [36] [61] [62], which states that if the thermal transient is sufficiently short, heat loss due to convection can be neglected. In the model, the thickness values being used are as follows: the paint thickness ranges from 0.01 to 10 mm (0.01 mm, 0.1 mm, 1 mm and 10 mm), while the steel thickness varies between 2.5 and 10 mm (2.5 mm, 5 mm, 7.5 mm, 10 mm). It is worth noting that standard spray paint applications typically do not exceed a few tenths of a millimeter in thickness. Nevertheless, we chose to investigate the thermal response behavior with paint layers up to 10 mm thick in order to gain a comprehensive understanding of their effects and to provide critical information for assessing the reliability of surface temperature measurements on painted surfaces.

2.2. Materials and preparation

Experimental tests on steel samples is employed to investigate the impact of paint coatings on both heating and cooling transients. A steel calibration block (Fig. 2(a)), commonly used for ultrasonic testing, was chosen as the test article.

The calibration block is made of 1018 carbon steel with uniform surface roughness (average of 5 measurements on base surface): Ra = 0.157 ± 0.018, Rq = 0.215 ± 0.021, Rt = 2.672 ± 0.650, Rz = 1.361 ± 0.118, Rp = 0.717 ± 0.120, Rv = 0.645 ± 0.121 µm. Roughness measurements were performed by means of a RTP80 rugosimiter with a cut-off of 0.8 mm and measurement length of 5 mm.

The test block consists of a series of steps with varying thicknesses (from 2.5 mm to 50 mm) while maintaining a constant width of 25 mm x

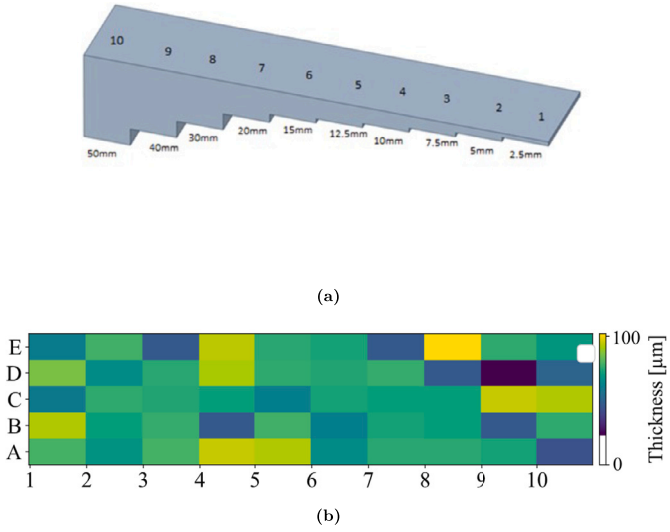

Fig. 2. Validation test piece (a) Step identification numbers for the tested thickness steps and (b) Heatmap showing the coating thickness distribution across the tested surface.

50 mm. This geometry allowed a direct comparison of thermal responses under identical heating conditions but different thicknesses.

The amount of energy actually deposited in the sample depends on the optical interaction between the laser and the surface. In heat transfer phenomena, if considering radiation (that is the energy transfer from laser to the target surface) there are three phenomena to take into consideration: transmission, reflection and absorption. Metallic substrates absorb only a limited fraction of the incident radiation, with the majority of the beam being reflected. For opaque surfaces transmission and reflection can be neglected [63]. Transmission phenomena are described by the Beer-Lambert's law [37][38][64], which are not taken into account in this model. In order to suppress reflection, the steel surface was first degreased with trichloroethylene and subsequently coated with a high-emissivity black paint, characterized by low reflectivity across the visible to far-infrared spectral range. The application of a high-emissivity black paint layer minimizes surface reflection, enhances infrared absorption, and ensures more accurate surface temperature measurements with the thermal camera. Since the coating is optically opaque, absorptance is effectively high and reflectivity can be safely neglected. Absorption becomes then dominant for the conservation of energy. The overall absorption is a function of wavelength and temperature which can both be assumed as constant as laser light is monocromatic and literature states in the investigated temperature ranges the emissivity value does not change in effective way [65,66]. Emissivity was measured according to the Standard [67] and found to be 0.6 for steel and 0.93 for paint coat-

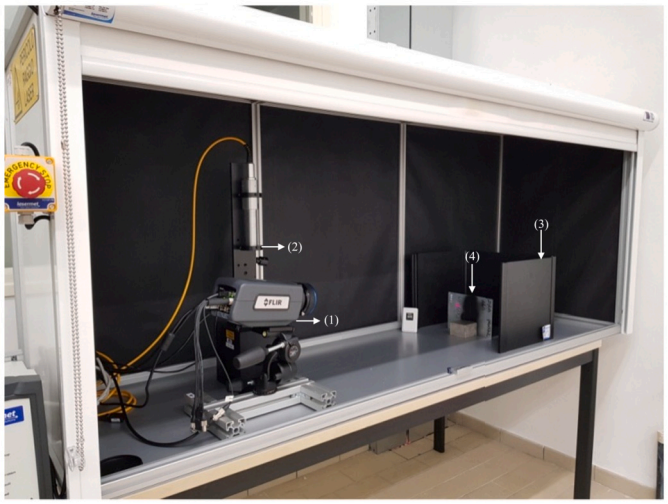

Fig. 3. Active thermography experimental setup with IR camera and laser source. (1) IR camera, (2) Laser, (3) protective panels, (4) test piece.

ing. The calculated emissivity data are consistent with values reported in the literature for two widely used coatings over comparable temperature ranges and wavelengths, showing only a modest dependence on temperature [66] [65].

The thickness of the paint layer was measured by means of coating thickness tester CG204 by EXTECH Instrumens (res. 0.1 μm). Thickness measurements of the paint layer showed an average layer of about 71.6 μm with a standard deviation of 15.7 μm, achieving a reasonably uniform coating (Fig. 2(b)).

2.3. Experimental setup

The temperature data was acquired using a thermal imaging system synchronized with the laser scanning head (Multi-DES), consisting in a IR thermal camera (FLIR A6751sc, sensitivity < 20 mK over a temperature range extending up to 1500 ∘ C, spectral range 3–5 μm, resolution of 640 × 512 pixels) and a pulsed laser from IPG Photonics (model YLPN-V2-1-100-50-50, 1064 nm wavelenght, max power 50 W with a gaussian beam profile 6 mm in diameter) (Fig. 3). The FLIR camera is built around an advanced Indium Antimonide (InSb) detector and its 50 mm lens, combined with a highly flexible integration time ranging from 480 ns to 687 sec, allows for precise control over exposure conditions. Moreover, the camera offers a programmable full-window frame rate from as low as 0.0015 Hz up to 125 Hz. The laser was focused on the bottom surface.

The laser power was set to 12.5 W power and 3 s on-time, delivering a total of 37.5 J of energy. Thermal maps were acquired at 100 Hz, ensuring a high temporal resolution. Testing was performed on painted bottom surface, targeting the center of each thickness step (Fig. 2(a)) and the thermal camera was positioned in reflection mode at a distance of 510 mm from the target surface (Fig. 3). All experiments were carried out under laboratory conditions, at room temperature (approximately 298 K, 25 °C).

Two region of interest (ROI) were selected, one around the laser spot (Fig. 4 in blue) to obtain the maximum temperature $T_{max}(t)$ for each step and one encompassing the entire step area (Fig. 4 in yellow) over which the average temperature $T_{aveSTEP}(t)$ was calculated for each step, enabling a comparison between local and global thermal responses. From the acquired thermograms, the two experimental key parameters, that are the maximum temperature increment $\Delta T_{max}(t)$ and the area-averaged temperature increment $\Delta T_{aveSTEP}(t)$ were extracted.

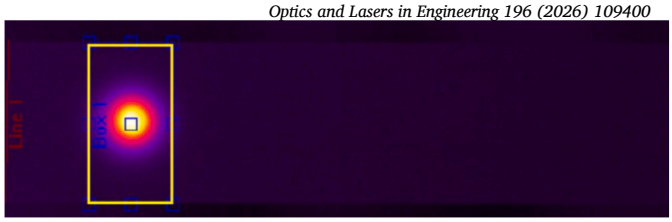

Fig. 4. Example of selected ROI for data extraction.

3. Results and discussion

The following section will report the results of the simulation and experiments. The time axis is interrupted at 10 s because stable trends are observed.

3.1. Effect of paint coating: analytical simulations

In Fig. 5 the temperature evolution in heating and cooling time intervals for the painted sample is reported, for different values of paint thickness (a = 0.01 mm, b = 0.1 mm, c = 1 mm, d = 10 mm) and of steel thickness (blue = 2.5 mm, orange = 5 mm, green = 7.5 mm, red = 10 mm, which correspond to the first 4 steps of our experimental tests).

It is shown that the paint layer adds both resistance and heat capacity, resulting in an initial temperature spike on the surface (Fig. 5). After this short transient, heat diffuses into the steel, and the long-term behavior aligns more closely with the substrate's properties.

Further parametric studies on paint and steel thickness variations (Fig. 5 and Fig. 6) confirmed that beyond certain thickness thresholds, the paint's influence hinders meaningful thickness discrimination. It is visible that for paint thicknesses over 1 mm the measurements overlaps. Moreover, from Fig. 6, can be seen how the paint produces a delay in the temperature increase. The Fig. 6 represents the temperature increase in the coupling surface between steel and paint, so, this measurement cannot be validated through experimental tests because the surface is not visible. For what concerns the steel temperature, it is worthy to observe that, for paint thickness 1 and 10 mm, the temperature in the steel continues to increase, also when the heat input is over, that is after, in this case, 3 seconds. This means that the thermal equilibrium between paint and steel is reached after a time interval which strongly depends on paint and steel thickness and of course on thermal input. For 10 mm paint thickness the simulated temperatures for both steel and paint surface tend to overlap, thus indicating different equilibrium balances take place.

3.2. Experimental results: influence of paint

The cooling phase of the thermal transient, particularly for the spatially averaged temperature, can be modeled by an exponential decay function:

$$\Delta T(t) = \Delta T_0 exp(-t/\tau) \tag{8}$$

where ΔT_0 is the initial temperature increment at the start of the cooling phase, and τ is the thermal time constant. This time constant encapsulates the combined effects of thermal resistance and capacitance, governing the rate at which the system returns to thermal equilibrium. It is inversely related to the thermal diffusivity and is dependent on the material's thickness, providing a quantitative link between the observed cooling behavior and the physical properties under investigation. A slower decay (larger τ) corresponds to a greater thermal mass or lower diffusivity, which is consistent with thicker samples. The ability to distinguish between different thicknesses is therefore contingent on resolving distinct τ values from the cooling curves.

In Fig. 7, the heating and cooling thermal profiles for maximum and average temperature in the ROIs are reported for the 7 steps undergo-

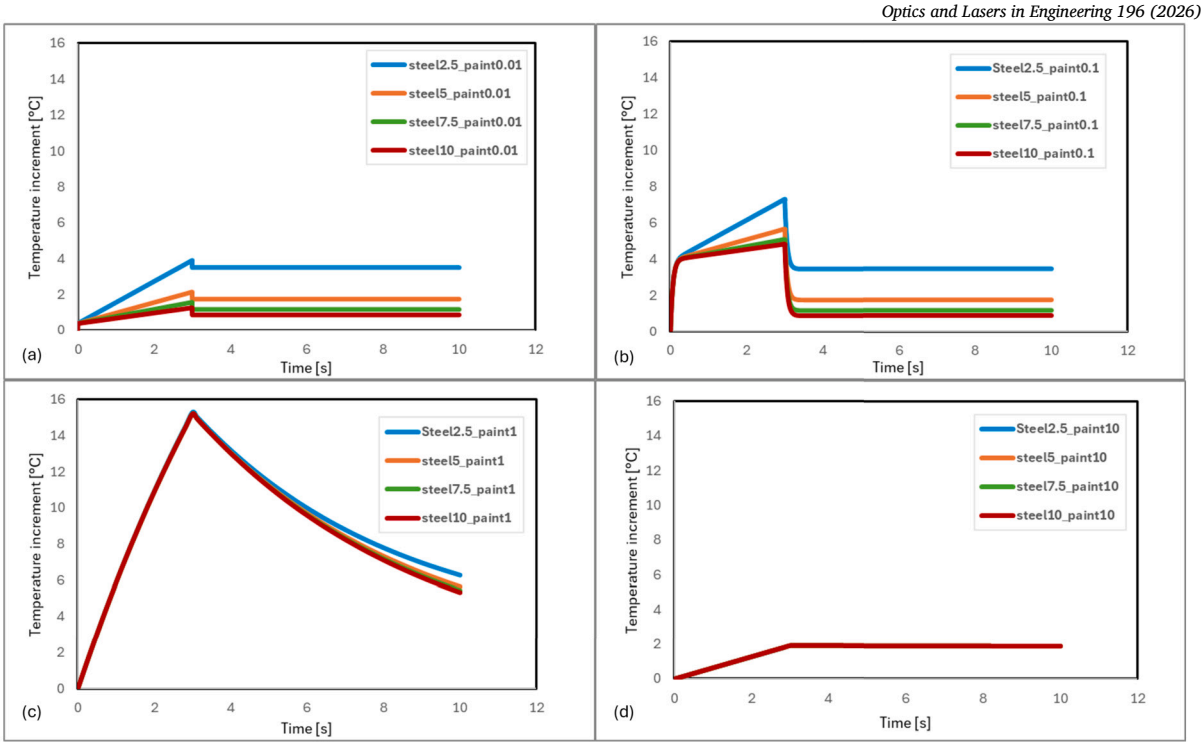

Fig. 5. Thermogram at the paint surface. Paint thickness: (a) 0.01 mm, (b) 0.1 mm, (c) 1 mm, (d) 10 mm; steel thickness: blue 2.5 mm, orange 5 mm, green 7.5 mm, red 10 mm.

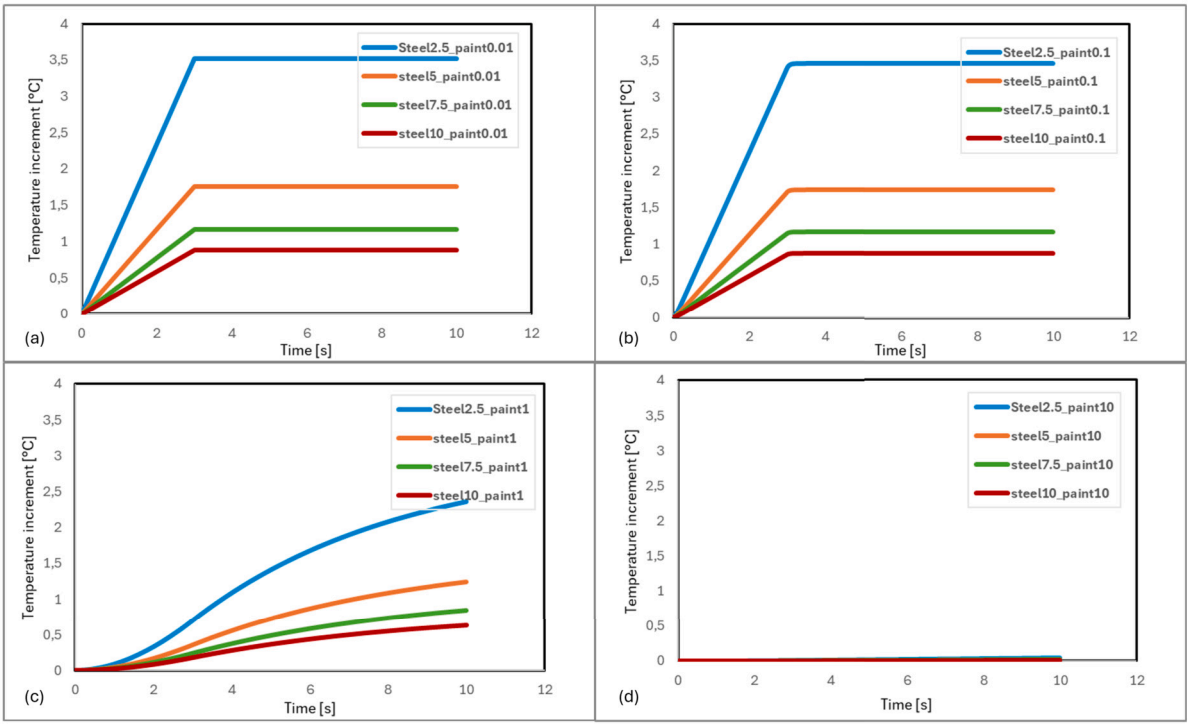

Fig. 6. Thermogram at the steel surface. Paint thickness: (a) 0.01 mm, (b) 0.1 mm, (c)1 mm, (d) 10 mm; steel thickness: blue 2.5 mm, orange 5 mm, green 7.5 mm, red 10 mm.

ing thermal laser pulses, for painted test piece. Tests carried out only up to step 7 have been reported because for higher thicknesses the thermal profiles tend to overlap. Experimental results on painted specimen showed a clear dependence of the temperature evolution on substrate thickness and the experimental curves related to average temperature increment are comparable with the simulated one. As shown in Fig. 7, thinner steps heat faster, reach higher peak temperatures and cool more slowly under the same input energy.

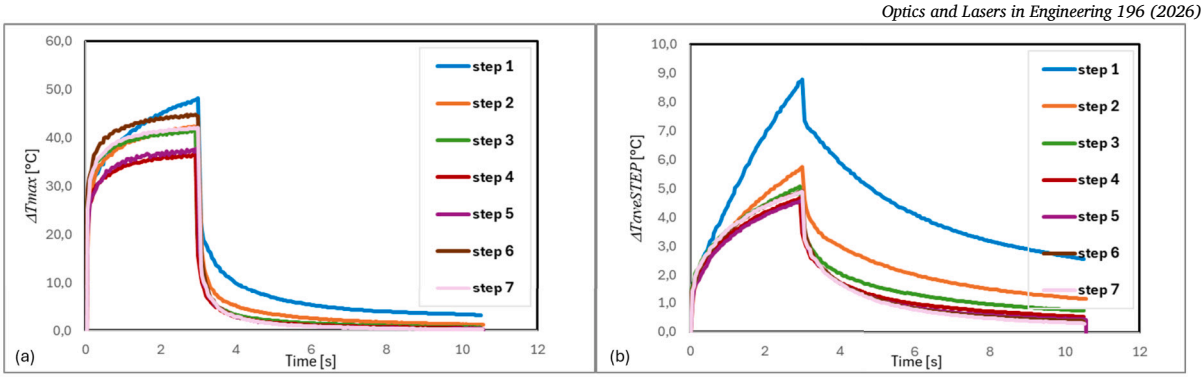

Fig. 7. Temperature evolution vs thickness: (a) maximum temperature evolution, (b) average temperature evolution.

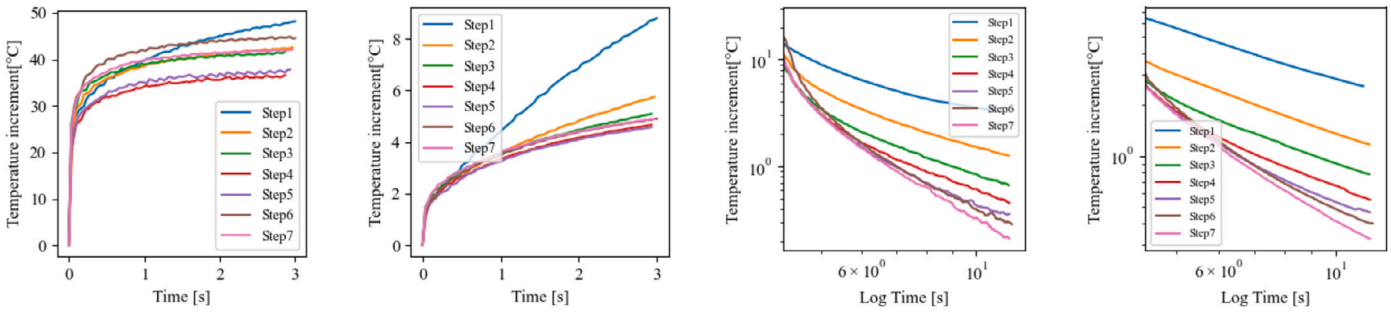

Fig. 8. (a) Maximum temperature increment during heating; (b) Average temperature increment during heating, averaged over the step surface.

Fig. 9. (a) Maximum temperature increment during cooling; (b) Average temperature increment during cooling, averaged over the step surface.

Fig. 7(b) refers to average temperature transient in heating and cooling profiles of painted test piece. In both profiles, a discontinuity is present, separating a steeper initial trend from a smoother subsequent trend. The steeper trend is referred to the evolution of the paint coating, indicating the paint role in altering the early transient.

Moreover, the temperature increment is way less than with the maximum temperature. This is related to the fact that the thermal heat source has a gaussian distribution, which in the averaged measurement is filtered.

The average temperature curves are expected to be comparable with the lumped model ones, since the simulated ones do not consider the non uniform (in space) heat input. Additionally, the maximum temperature may suffer from non uniform photothermal properties of the surface, and in particular corrosion spots, reflections and superficial scratches may affect the maximum temperature measurement.

Therefore, the transient curves are split between the heating and cooling parts. In order to highlight differences, the cooling curves are presented in logarithmic scale. As regards the maximum temperature increases, both heating and cooling, by analyzing all thickness steps under painted conditions (Fig. 8(a) and Fig. 9(a)), it becomes evident that the early heating phase is dominated by paint properties, obscuring thickness differences. In contrast, the cooling phase allows some thickness discrimination up to about 10 mm. Beyond this limit, the curves overlap, and thickness differences are no longer distinguishable.

Moreover, spatial averaging over the entire step area helps in partially recovering thickness discrimination. Fig. 8(b) and Fig. 9(b) show that when considering the broader area, distinct thermal profiles remain visible for thicknesses up to around 10 mm. For thicker steps, the paint's thermal inertia combined with the larger steel volume masks the differences. Both for maximum and averaged temperature, however, the cooling curve follows a robust trend with respect to the steel thickness. As expected, the mean temperature cooling curves (Fig. 9(b)) are smoother and more distinct.

3.3. Lumped parameter model validation

Fig. 10 shows the average temperature increase from step 1 (2.5 mm) to step 4 (10 mm of steel), comparing the simulation curves for both the test piece surface (Tpaint) and the coupling surface (Tsteel) with the experimental curves for the individual steps. The experimental curves related to average temperature increment is comparable with the simulated ones referred to paint temperature. This because the lumped parameter is 0D and it assumes a uniform temperature distribution on the step area. The different slope trend can be attributed to different effects. First of all the lumped parameter model considers a perfect square wave lasting 3 seconds. The experimental laser wave has last a 3 second interval with starting and ending transients which deviate the temporal square shape. Compared to the 3 second wave interval, we assumed that these transients neglectable and not requiring a detailed simulation. Other effects are non simulated experimental setup discrepancies, for example non uniform heating, corrosion spots and superficial scratches may affect the temperature measurement.

4. Extended discussion and practical implications

The key takeaway is that while black paint coatings stabilize emissivity and reduce reflections, they introduce a short-time transient masking effect. For applications requiring thickness discrimination—such as evaluating thin-walled structures, detecting small defects, or characterizing layered materials—this masking can reduce the reliability of AT measurements.

Potential strategies to mitigate these issues include:

- Using thinner or more conductive paint coatings to minimize the initial transient distortion.
- Analyzing data over time intervals that exceed the initial transient, focusing on the part of the curve where substrate properties dominate.

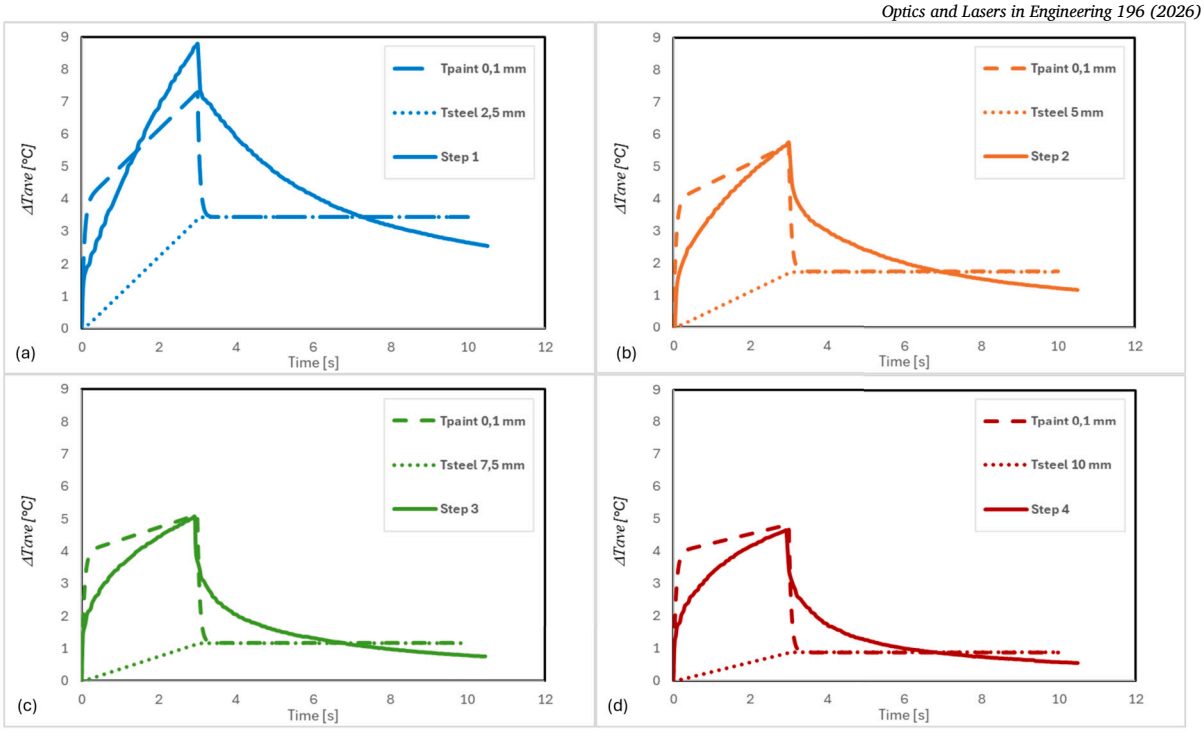

Fig. 10. Average Temperature increment simulated vs experimental: (a) step 1 (steel 2.5 mm), (b) step 2 (steel 5 mm), (c) step 3 (steel 7.5 mm), (d) step 4 (steel 10 mm).

- Applying spatial averaging or advanced signal processing techniques (e.g., inverse methods, machine learning) to filter out the coating-induced artifacts.

In industrial contexts where coatings are standard—such as corrosion protection layers on marine or aerospace components—understanding and compensating for these effects is essential. The results presented here provide a framework to approach data interpretation, guiding users to adjust data processing strategies or experimental parameters to maintain reliable thickness differentiation.

5. Conclusions

This study has quantitatively demonstrated the significant masking effect that a high-emissivity paint coating can have on the ability of laser-long pulse active thermography to discriminate substrate thickness. Our integrated approach, combining analytical modeling, numerical simulation, and experimental validation, leads to the following key conclusions:

- **Coating-Induced Transient Masking:** The low thermal diffusivity of the paint layer induces a rapid initial temperature spike that dominates the early thermal transient, effectively masking the more subtle, thickness-dependent response of the steel substrate. This effect is a direct consequence of the thermal barrier created by the coating.
- **Limits of Thickness Discrimination:** We have established a practical thickness discrimination threshold of approximately 10 mm for the coated steel samples under our experimental conditions. Beyond this threshold, the thermal responses of different thicknesses become indistinguishable, even with the use of spatial averaging.
- **Efficacy of Mitigation Strategies:** Spatial averaging of the temperature data and focusing on the later cooling phase have been shown to be effective strategies for partially mitigating the masking effect. These methods help to filter out localized noise and emphasize the bulk thermal behavior of the substrate, thereby improving the signal-to-noise ratio for thickness discrimination.
- **Practical Implications for NDE:** The findings underscore the critical need for careful consideration of coating properties in any quantitative application of active thermography. For reliable NDE, practitioners must either select coatings with thermal properties that minimize transient masking (e.g., thin, high-conductivity layers) or employ advanced data analysis techniques to deconvolve the coating's influence from the measured signal.

In summary, while emissivity-enhancing coatings are indispensable for many thermographic applications, their thermal properties are not benign. A thorough understanding of the trade-off between improved emissivity and transient masking is essential for ensuring the accuracy and reliability of active thermography as a quantitative NDE tool.

CRediT authorship contribution statement

Raffaella Sesana: Writing – review & editing, Writing – original draft, Visualization, Supervision, Project administration, Funding acquisition, Formal analysis, Conceptualization. **Luca Santoro:** Writing – review & editing, Writing – original draft, Visualization, Validation, Software, Methodology, Investigation, Formal analysis, Conceptualization. **Ludovica Tromba:** Writing – review & editing, Writing – original draft, Visualization, Validation, Software, Data curation.

Funding

Not applicable.

Declaration of competing interest

The authors declare the following financial interests/personal relationships which may be considered as potential competing interests: Ludovica Tromba reports financial support was provided by Italian Ministry of University and Research (PNRR-NGEU, MUR-DM630/2024). If there are other authors, they declare that they have no known competing financial interests or personal relationships that could have appeared to influence the work reported in this paper.

Acknowledgements

This publication is part of the project PNRR-NGEU which has received funding from the MUR–DM630/2024.

Data availability

Data will be made available on request.

References

[1] Vavilov V, Burleigh D. Infrared thermography and thermal nondestructive testing. Infrared Thermogr Therm Nondestruct Test 2020;1(598). https://doi.org/10.1007/978-3-030-48002-8.

[2] Siddiqui JA, Arora V, Mulaveesala R, Muniyappa A. Infrared thermal wave imaging for nondestructive testing of fibre reinforced polymers. Exp Mech 2015;55(7):1239–45. https://doi.org/10.1007/S11340-015-0019-Z.

[3] Carvalho MS, Martins AP, Santos TG. Simulation and validation of thermography inspection for components produced by additive manufacturing. Appl Therm Eng 2019;159:113872. https://doi.org/10.1016/j.applthermaleng.2019.113872.

[4] Tang Q, Dai J, Bu C, Qi L, Li D. Experimental study on debonding defects detection in thermal barrier coating structure using infrared lock-in thermographic technique. Appl Therm Eng 2016;107:463–8. https://doi.org/10.1016/j.applthermaleng.2016.07.008.

[5] Bang HT, Park S, Jeon H. Defect identification in composite materials via thermography and deep learning techniques. Compos Struct 2020;246. https://doi.org/10.1016/j.compstruct.2020.112405.

[6] Huang KL, Sfarra S, Wen CM, Yao Y, Zhao C. Exploratory factor analysis for defect identification with active thermography. Meas Sci Technol 2021;32(11). https://doi.org/10.1088/1361-6501/ac17f9.

[7] Maierhofer C, Röllig M, Steinfurth H, Ziegler M, Kreutzbruck M, Scheuerlein C, et al. Non-destructive testing of Cu solder connections using active thermography. NDT E Int 2012;52:103–11. https://doi.org/10.1016/j.ndteint.2012.07.010.

[8] Sirikham A, Zhao Y, Liu H, Xu Y, Williams S, Mehnen J. Three-dimensional subsurface defect shape reconstruction and visualisation by pulsed thermography. Infrared Phys Technol 2020;104(2019):103151. https://doi.org/10.1016/j.infrared.2019.103151.

[9] Silva WF, Melo RAC, Grosso M, Pereira GR, Riffel DB. Active thermography data-processing algorithm for nondestructive testing of materials. IEEE Access 2020;8:175054–62. https://doi.org/10.1109/ACCESS.2020.3025329.

[10] Meng X, Wang Y, Liu J, He W. Nondestructive inspection of curved clad composites with subsurface defects by combination active thermography and three-dimensional (3D) structural optical imaging. Infrared Phys Technol 2019;97:424–31. https://doi.org/10.1016/j.infrared.2019.01.026.

[11] Grys S, Vokorokos L, Borowik L. Size determination of subsurface defect by active thermography - simulation research. Infrared Phys Technol 2014;62:147–53. https://doi.org/10.1016/j.infrared.2013.11.011.

[12] Hagqvist P, Sikström F, Christiansson AK, Lennartson B. Emissivity compensated spectral pyrometry for varying emissivity metallic measurands. Meas Sci Technol 2014;25(2):8. https://doi.org/10.1088/0957-0233/25/2/025010.

[13] Pitarresi G, Cappello R, Capraro A, Pinto V, Badagliacco D, Valenza A. Frequency modulated thermography-NDT of polymer composites by means of human-controlled heat modulation. Lect. Notes Civ. Eng., vol. 254. LNCE; 2023. p. 610–8.

[14] Borghese V, Santoro L, Santini S, Sesana R. Correlation between thermal and density properties of chestnuts: preliminary results of experimental non-destructive testing. Arch Civ Mech Eng 2024;24(3):1–15. https://doi.org/10.1007/s43452-024-00969-8.

[15] Runnemalm A, Ahlberg J, Appelgren A, Sjökvist S. Automatic inspection of spot welds by thermography. J Nondestruct Eval 2014;33(3):398–406. https://doi.org/10.1007/s10921-014-0233-0.

[16] Jonietz F, Myrach P, Suwala H, Ziegler M. Examination of spot welded joints with active thermography. J Nondestruct Eval 2016;35(1):1–14. https://doi.org/10.1007/s10921-015-0318-4.

[17] Roemer J, Pieczonka Ł, Uhl T. Laser spot thermography of welded joints. Diagnostyka 2014;15(2):43–9.

[18] Salazar A, Celorrio R. Application of the thermal quadrupole method to the propagation of thermal waves in multilayered cylinders. J Appl Phys 2006;100(11). https://doi.org/10.1063/1.2400403.

[19] Salazar A, Mendioroz A, Oleaga A. Flying spot thermography: quantitative assessment of thermal diffusivity and crack width. J Appl Phys 2020;127(13). https://doi.org/10.1063/1.5144972.

[20] Philipp A, Pech-May NW, Kopera BAF, Lechner AM, Rosenfeldt S, Retsch M. Direct measurement of the in-plane thermal diffusivity of semitransparent thin films by lock-in thermography: an extension of the slopes method. Anal Chem 2019;91(13):8476–83. https://doi.org/10.1021/acs.analchem.9b01583.

[21] Li T, Almond DP, Rees DAS. Crack imaging by scanning pulsed laser spot thermography. NDT E Int 2011;44(2):216–25. https://doi.org/10.1016/j.ndteint.2010.08.006.

[22] Zhou Q, Rong Y, Shao X, Jiang P, Gao Z, Cao L. Optimization of laser brazing onto galvanized steel based on ensemble of metamodels. J Intell Manuf 2018;29(7):1417–31. https://doi.org/10.1007/s10845-015-1187-5.

[23] Kato H, Baba T, Okaji M. Anisotropic thermal-diffusivity measurements by a new laser-spot-heating technique. Meas Sci Technol 2001;12(12):2074–80. https://doi.org/10.1088/0957-0233/12/12/307.

[24] Wolf A, Pohl P, Brendel R. Thermophysical analysis of thin films by lock-in thermography. J Appl Phys 2004;96(11):6306–12. https://doi.org/10.1063/1.1811390.

[25] Ishizaki T, Nagano H. Measurement of three-dimensional anisotropic thermal diffusivities for carbon fiber-reinforced plastics using lock-in thermography. Int J Thermophys 2015;36(10–11):2577–89. https://doi.org/10.1007/s10765-014-1755-5.

[26] Maierhofer C, Myrach P, Krankenhagen R, Röllig M, Steinfurth H. Detection and characterization of defects in isotropic and anisotropic structures using lockin thermography. J Imaging 2015;1(1):220–48. https://doi.org/10.3390/jimaging1010220.

[27] Guo X, Vavilov V. Crack detection in aluminum parts by using ultrasound-excited infrared thermography. Infrared Phys Technol 2013;61:149–56. https://doi.org/10.1016/j.infrared.2013.08.003.

[28] Srajbr C. Induction excited thermography in industrial applications; 2016. p. 1–9.

[29] Apiñaniz E, Mendioroz A, Madariaga N, Oleaga A, Celorrio R, Salazar A. Thermal characterization of rods, tubes and spheres using pulsed infrared thermography. J Phys D, Appl Phys 2008;41(1). https://doi.org/10.1088/0022-3727/41/1/015403.

[30] Vv Aa. Il giornale delle prove non distruttive monitoraggio diagnostica. G. delle prove non distruttive monit. Diagnostica 2010;4.

[31] Sadiq H, Wong MB, Tashan J, Al-Mahaidi R, Zhao X-L. Determination of steel emissivity for the temperature prediction of structural steel members in fire. J Mater Civ Eng 2013;25(2):167–73. https://doi.org/10.1061/(asce)mt.1943-5533.0000607.

[32] Honner M, Litoš P, Švantner M. Thermography analyses of the hole-drilling residual stress measuring technique. Infrared Phys Technol 2004;45(2):131–42. https://doi.org/10.1016/j.infrared.2003.08.001.

[33] Rajic N, Antolis C. An investigation of noise performance in optical lock-in thermography. Infrared Phys Technol 2017;87:1–10. https://doi.org/10.1016/j.infrared.2017.09.019.

[34] Susa M, Maldague X, Svaic S, Boras I, Bendada A. The influence of surface coatings on the differences between numerical and experimental results for samples subjected to pulse thermography examination. https://doi.org/10.21611/qirt.2008.12_11_16, 2008.

[35] International Organization for Standardization: Metallic and Other Inorganic Coatings — Determination of Thermal Conductivity of Thermal Barrier Coatings. Geneva, Switzerland. 2016. ISO 18555:2016.

[36] International Organization for Standardization: Fine Ceramics [advanced Ceramics, Advanced Technical Ceramics] — Determination of Thermal Diffusivity of Monolithic Ceramics by Laser Flash Method. 2004. ISO 18755:2004(E).

[37] Wang H, Kawahito Y, Yoshida R, Nakashima Y, Shiokawa K. A model to calculate the laser absorption property of actual surface. Int J Heat Mass Transf 2018;118:562–9. https://doi.org/10.1016/j.ijheatmasstransfer.2017.11.023.

[38] Rudolf C, Manzo M, Mathews S, Rogers D. A novel laser-based high temperature mechanical property characterization method. Mater Charact 2025;228:115393. https://doi.org/10.1016/j.matchar.2025.115393.

[39] Bagavathiappan S, Lahiri BB, Saravanan T, Philip J, Jayakumar T. Infrared thermography for condition monitoring - a review (2013). https://doi.org/10.1016/j.infrared.2013.03.006, 2013.

[40] Schlichting J, Brauser S, Pepke LA, Maierhofer C, Rethmeier M, Kreutzbruck M. Thermographic testing of spot welds. NDT E Int 2012;48:23–9. https://doi.org/10.1016/j.ndteint.2012.02.003.

[41] Sommier A, Malvaut J, Delos V, Romano M, Bazire T, Batsale JC, et al. Coupling pulsed flying spot technique with robot automation for industrial thermal characterization of complex shape composite materials. NDT E Int 2019;102:175–9. https://doi.org/10.1016/j.ndteint.2018.11.011.

[42] Parker WJ, Jenkins RJ, Butler CP, Abbott GL. Flash method of determining thermal diffusivity, heat capacity, and thermal conductivity. J Appl Phys 1961;32(9):1679–84. https://doi.org/10.1063/1.1728417.

[43] Doshvarpassand S, Wu C, Wang X. An overview of corrosion defect characterization using active infrared thermography. Elsevier B.V.; 2019.

[44] Santoro L, Quercio M, Canova A, Sesana R. Measuring thermal and electrical performances of additively manufactured magnetic shielding material: an active thermography approach. Nondestruct Test Eval 2024:1–24. https://doi.org/10.1080/10589759.2024.2305703.

[45] Quercio M, Del Pino Lopez JC, Grasso S, Canova A. Numerical and experimental analysis of thermal behaviour of high voltage power cable in unfilled ducts. Sci Rep 2024;14(1). https://doi.org/10.1038/S41598-024-71281-X.

[46] Dell'Avvocato G, Palumbo D, Pepe R, Galietti U. Non-destructive evaluation of resistance projection welded joints (RPW) by flash thermography. IOP Conf Ser, Mater Sci Eng 2021;1038(1):012003. https://doi.org/10.1088/1757-899x/1038/1/012003.

[47] Dell'Avvocato G, Palumbo D, Galietti U. A non-destructive thermographic procedure for the evaluation of heat treatment in Usibor®1500 through the thermal diffusivity measurement. NDT E Int 2023;133. https://doi.org/10.1016/j.ndteint.2022.102748.

[48] D'Accardi E, De Finis R, Dell'Avvocato G, Masciopinto G, Palumbo D, Galietti U. Conduction thermography for non-destructive assessment of fatigue cracks in metallic materials. Infrared Phys Technol 2024;140:105394. https://doi.org/10.1016/j.infrared.2024.105394.

[49] Sesana R, Santoro L, Curà F, Molica Nardo R, Pagano P. Assessing thermal properties of multipass weld beads using active thermography: microstructural variations and anisotropy analysis. Int J Adv Manuf Technol 2023;128(5–6):2525–36. https://doi.org/10.1007/s00170-023-11951-8.

[50] Walther HG, Fournier D, Krapez JC, Luukkala M, Schmitz B, Sibilia C, et al. Photothermal steel hardness measurements - results and perspectives. Anal Chem 2001;17:165–8.

[51] García de la Yedra A, Fernández E, Beizama A, Fuente R, Echeverria A, Broberg P, et al. Defect detection strategies in Nickel Superalloys welds using active thermography. QIRT Council; 2014.

[52] Strzałkowski K, Streza M, Dadarlat D, Marasek A. Thermal characterization of II-VI binary crystals by photopyroelectric calorimetry and infrared lock-in thermography. J Therm Anal Calorim 2015;119(1):319–27. https://doi.org/10.1007/s10973-014-4137-0.

[53] Raab SJ, Guschlbauer R, Lodes MA, Körner C. Thermal and electrical conductivity of 99.9% pure copper processed via selective electron beam melting. Adv Eng Mater 2016;18(9):1661–6. https://doi.org/10.1002/adem.201600078.

[54] Liu Y, Sun T, Wang C, Mandelis A. Quantitative photothermal lock-in thermography imaging of curved surfaces of cylindrical solids. J Appl Phys 2020;127(19). https://doi.org/10.1063/5.0007779.

[55] Matarrese T, Palumbo D, Galietti U. Comparison in the transient regime of four lock-in thermography algorithms by means of synthetic and experimental data on CFRP. NDT E Int 2023;139:102925. https://doi.org/10.1016/j.ndteint.2023.102925.

[56] Ishizaki T, Nagano H, Tanaka S, Sakatani N, Nakamura T, Okada T, et al. Measurement of microscopic thermal diffusivity distribution for Ryugu sample by infrared lock-in periodic heating method. Int J Thermophys 2023;44(4). https://doi.org/10.1007/s10765-023-03158-6.

[57] Canova A, Tartaglia M, Quercio M. Optimisation design of a low-frequency eddy current rail heater. Energies 2023;16(21). https://doi.org/10.3390/en16217427.

[58] Stella M, Faba A, Fulginei FR, Quercio M, Scorretti R, Bertolini V, et al. Experimental measurements and numerical modelling of additively manufactured Fe-Si cores. J Magn Magn Mater 2024;591. https://doi.org/10.1016/J.JMMM.2024.171752.

[59] Panas AJ, Szczepaniak R, Strycznieiwcz W, Omen Ł. Thermophysical properties of temperature-sensitive paint. Materials (Basel) 2021;14(8). https://doi.org/10.3390/ma14082035.

[60] Wielgosz E, Kargul T, Falkus J. Comparison of experimental and numerically calculated thermal properties of steels. In: Met. 2014 - 23rd int. conf. metall. mater. conf. proc.; 2014. p. 1528–33.

[61] Japanese Standards Association: Testing methods of thermal diffusivity, specific heat capacity and thermal conductivity for high performance ceramics by laser flash method. JIS R 1611:1991. Japanese Industrial Standard (1991).

[62] Cernuschi F, Russo A, Lorenzoni L, Figari A. In-plane thermal diffusivity evaluation by infrared thermography. Rev Sci Instrum 2001;72(10):3988–95. https://doi.org/10.1063/1.1400151.

[63] Howell JR, Mengüç MP, Siegel R. Thermal radiation heat transfer. 6th edn. Boca Raton, FL: CRC Press, Taylor & Francis Group; 2016.

[64] Brown MS, Arnold CB. Fundamentals of laser-material interaction and application to multiscale surface modification. Laser precision microfabrication. Springer series in materials science, vol. 135. Berlin, Heidelberg: Springer; 2010. p. 91–120.

[65] Mankiewicz Gebr. & Co. (GmbH & Co. KG): NEXTEL Velvet-Coating 811-21 Technical Datasheet. Mankiewicz Gebr. & Co. (GmbH & Co. KG), Hamburg, Germany. Revision 2, March 9, 2021 (2021).

[66] Adibekyan A, Kononogova E, Monte C, Hollandt J. High-accuracy emissivity data on the coatings nextel 811-21, herberts 1534, aeroglaze Z306 and acktar fractal black. Int J Thermophys 2017;38(89):1–14. https://doi.org/10.1007/s10765-017-2212-z.

[67] ASTM International. Standard Practice for Measuring and Compensating for Emissivity Using Infrared Imaging Radiometers. Standard Practice. 2014. ASTM Standard E1933-14.